ON THE TVD PROPERTY OF SECOND ORDER METHODS FOR TWO-DIMENSIONAL SCALAR CONSERVATION LAWS

LILIA KRIVODONOVA AND ALEXEY SMIRNOV

Abstract. The total variation diminishing (TVD) property is an important tool for ensuring nonlinear stability and convergence of numerical solutions of one-dimensional scalar conservation laws. However, it proved to be challenging to extend this approach to two-dimensional problems. Using the anisotropic definition for discrete total variation (TV), it was shown in [14] that TVD solutions of two-dimensional hyperbolic equations are at most first order accurate. We propose to use an alternative definition resulting from a full discretization of the semi-discrete Raviart-Thomas TV. We demonstrate numerically using the second order discontinuous Galerkin method that limited solutions of two-dimensional hyperbolic equations are TVD in means when total variation is computed using the new definition.

Keywords. Hyperbolic conservation laws, total variation diminishing schemes, discontinuous Galerkin method, high-order methods.

1. Introduction

We consider two-dimensional hyperbolic scalar conservation laws

$$u_t + f(u)_x + g(u)_y = 0, \tag{1}$$

where f and g are the flux components in the x- and y-directions, respectively. Weak solutions of (1) might develop discontinuities in finite time even with smooth initial data. This is one of the challenges in designing robust numerical methods for these equations. Modern methods, which are formally at least second order accurate, develop spurious oscillations near solution discontinuities that need to be controlled in order for the solution to remain stable. At the same time, suppressing oscillations should not substantially reduce solution accuracy in the rest of the domain. For one-dimensional problems, this issue has been largely resolved by enforcing the total variation diminishing (TVD) property [15]. Let U^n be a numerical solution to (1) at $t = t^n$. A one-step numerical scheme $U^{n+1} = F(U^n)$ is called total variation diminishing (TVD) if U^n satisfies the following condition

$$TV(U^{n+1}) \leq TV(U^n), \quad \forall n. \tag{2}$$

Let $\Omega \in \mathbb{R}^2$ be a bounded open set and $u \in L_1(\Omega)$. Then the total variation $TV(u)$ is defined as [8]

$$TV(u) = \sup_{\boldsymbol{\varphi} \in C_c^1(\Omega)} \left\{ -\int_\Omega u \nabla \cdot \boldsymbol{\varphi} \, dxdy : \|\boldsymbol{\varphi}(x,y)\| \leq 1, \forall (x,y) \in \Omega \right\}, \tag{3}$$

where $\|\boldsymbol{\varphi}(x,y)\| = \sqrt{\varphi^2(x,y) + \psi^2(x,y)}$ and $\boldsymbol{\varphi}(x,y)$ is a differentiable vector function. For sufficiently smooth functions u, e.g. $u \in W^{1,1}(\Omega)$, where $W^{1,1}(\Omega)$ is a Sobolev space, the definition (3) reduces to

$$TV(u) = \int_\Omega \sqrt{u_x^2 + u_y^2} \, dxdy. \tag{4}$$

Several definitions of discrete TV, i.e. TV for functions defined on a computational grid, have been proposed in the literature. Let us assume that Ω is a rectangular domain discretized into a Cartesian grid of elements $\Omega_{i,j} = [x_{i-1/2}, x_{i+1/2}] \times [y_{j-1/2}, y_{j+1/2}]$ with centroids at points $(x_i,\, y_j)$ and the grid sizes in the x and y directions $\Delta x_i = x_{i+1/2} - x_{i-1/2}$ and $\Delta y_j = y_{j+1/2} - y_{j-1/2}$, respectively. Let U be a discrete function defined on this grid with $U_{i,j}$ being the value associated with element $\Omega_{i,j}$.

In their classical work, Goodman and LeVeque [14] used discrete TV of the form

$$TV_a(U) = \sum_{i,j} \Big(\Delta y_j |U_{i+1,j} - U_{i,j}| + \Delta x_i |U_{i,j+1} - U_{i,j}| \Big), \tag{5}$$

Date: Department of Applied Mathematics, University of Waterloo, June 2021.

commonly referred to in the literature as anisotropic TV. The definition (5) is a discrete approximation of

$$TV_a(u) = \int_\Omega |u_x| + |u_y| \; dxdy. \tag{6}$$

They showed that any conservative, TVD scheme for solving hyperbolic conservation laws in the two-dimensional space is at most first-order accurate for monotone solutions of (1). In order to prove this statement, an associated one-dimensional scheme with the same order of accuracy and special initial data was considered. If the two-dimensional scheme is TVD, then the corresponding one-dimensional scheme should be monotone at least on certain initial data and, therefore, is at most first-order accurate. Thus, the original two-dimensional scheme is also at most first order accurate.

The TVD property is an important tool for proving nonlinear stability and convergence of a numerical scheme for one-dimensional problems. The limiters are commonly used to develop TVD schemes, e.g. [19, 24] for finite volume methods and [6] for DG methods. In the absence of a suitable TVD property for higher order two-dimensional schemes, most proposed and currently in use limiters are ad hoc. Recently, the local maximum principle (LMP) has been employed in proving stability of numerical solutions in the maximum norm [10, 11, 12, 13, 18]. The LMP property that the solution averages on a computational element at the next time level will not exceed the bounds given by solution averages at the present time in some neighborhood of the element. Thus, the solution is stable in the maximum norm for all times. Unfortunately, stability in the maximum norm is not sufficient to guarantee convergence, though enforcing both linear stability and LMP is property resulted in a convergent scheme [10]. Therefore, it is desirable to develop a TVD definition, that once enforced on solutions of high-order schemes, will guarantee stability and convergence.

While no two-dimensional numerical scheme can be both TVD and second order accurate in the sense of (5), this statement was not proven for all possible definitions of discrete TV, e.g. a widely used

$$TV_{is}(U) = \sum_{i,j} \sqrt{\Delta y_j^2 \left(U_{i+1,j} - U_{i,j}\right)^2 + \Delta x_i^2 \left(U_{i,j+1} - U_{i,j}\right)^2}, \tag{7}$$

which was first introduced in [23], and is commonly referred to in the literature as isotropic TV. The analytical TV defined by (3) is translation and rotation-invariant. However, the discrete TV definitions (5) and (7) are not isotropic, i.e. if the shape given by u is rotated, the corresponding values of $TV_a(U)$, $TV_{is}(U)$ can increase or decrease, see [7] and Section 3. This makes these definitions not suitable for our purposes, since the TV of the numerical solution of (1) will depend on the orientation of u with respect to the grid. Both (5) and (7) are based on the forward difference approximations of ∇u, and while (7) improves the accuracy of (5), it remains spatially anisotropic. A comprehensive discussion of this issue can be found in [2].

A novel approach to computing discrete TV has been recently proposed in [16]. Given a mesh, the authors considered a staggered grid approximation of the divergence operator in (3) and solved an optimization problem to find $TV(U)$. This approach, mimicking the standard, by duality, definition of the total variation, is referred to as the discrete dual TV. Since $TV(u)$ is a convex functional for $u \in L_1(\Omega)$, the optimization problem resulting from discretization of (3) has a unique global maximum, and can be solved by many standard proximal algorithms for convex optimization. The convergence of discrete dual TV to (3) holds in both weak and strong topologies, e.g. $L_p(\Omega)$ for any $p < +\infty$, [4, 5]. Moreover, for a broad family of discrete dual TV [4] any sequence of bounded in L_p discrete functions, with uniformly bounded dual TV contains a convergent subsequence. A fast proximal gradient descent algorithm for solving the optimization problem arising from the implementation of this formulation was proposed in [16] and further improved in [7]. The new dual discrete TV led to improvement in accuracy of TV computation and was used to solve TV-regularization based optimization problems with applications to image denoising, inpainting, motion estimation, and multi-label image segmentation [20, 7, 1, 21, 3].

The main features distinguishing duality based TV definitions from the classical (5) and (7) are spatial isotropy and asymptotic consistency with (3). Among multiple dual discrete definitions, the one proposed in [7] is the most "isotropic" according to [5]. However, it is difficult to define the isotropy of a discrete TV, since there is no unique way of defining rotation and translation on a mesh.

In this paper, we consider TV_a, TV_{is}, and the novel dual definition and apply them to compute TV in means of numerical solutions of two-dimensional hyperbolic equations. In particular, we employ the

second order discontinuous Galerkin method with the moment limiter [17]. We demonstrate that the computed numerical solutions are not TVD in the TV_a and TV_{is} sense, as expected. In contrast, the means of limited numerical solutions remain TVD when the dual definition is used. We conjecture that similar to one-dimensional problems, common limiters that are known in practice to stabilize solutions, reduce the slope of the solution enough for it to be TVD in the dual sense. Thus, we propose to use the dual TV definition as a suitable measure of multi-dimensional discrete TV for solutions of PDEs.

The paper is organized as follows. Section 2 introduces the duality-based definitions of discrete total variation and the algorithms used to compute it. Section 3 contains two numerical tests, which are used to compare the isotropy, accuracy, and consistency of the discrete TVs described above. The main numerical results are presented in Section 4 where we use the discontinuous Galerkin method to compute solutions to (1) and their TVs. Finally, Section 5 presents our conclusions.

2. Duality-based discrete TV definitions

In this section we introduce duality-based definitions of discrete TV. Let $u \in L_1(\Omega)$ have a bounded distributive derivative Du, and let a test function $\boldsymbol{\varphi} = (\varphi, \psi)$ be a differentiable vector field. We will further assume that $\|\boldsymbol{\varphi}(x,y)\| \le 1,\ \forall (x,y) \in \Omega$, and $(\boldsymbol{\varphi} \cdot \vec{\boldsymbol{n}}) = 0$ on $\partial\Omega$, where $\vec{\boldsymbol{n}}$ is the unit normal vector along the boundary $\partial\Omega$. Then by the divergence theorem the following identity holds

$$\int_\Omega u \nabla \cdot \boldsymbol{\varphi}\ dxdy = -\int_\Omega \boldsymbol{\varphi} Du\ dxdy. \tag{8}$$

Note that Du can be replaced by ∇u if u is sufficiently smooth [9]. Using (8) in (3), the total variation of u on Ω can be defined as

$$TV(u) = \sup_{\boldsymbol{\varphi} \in C_c^1(\Omega)} \left\{ \int_\Omega \boldsymbol{\varphi} Du\ dxdy : \|\boldsymbol{\varphi}(x,y)\| \le 1,\ \forall (x,y) \in \Omega \right\}. \tag{9}$$

We can approximate the left hand side of (8) as

$$\int_\Omega u \nabla \cdot \boldsymbol{\varphi}\ dxdy \approx \sum_{i,j} u_{i,j} \left(\frac{\varphi_{i+1/2,j} - \varphi_{i-1/2,j}}{\Delta x_i} + \frac{\psi_{i,j+1/2} - \psi_{i,j-1/2}}{\Delta y_j} \right) \Delta x_i \Delta y_j, \tag{10}$$

where $\varphi_{i+1/2,j} = \varphi(x_{i+1/2}, y_j)$, $\psi_{i,j+1/2} = \psi(x_i, y_{j+1/2})$, $\varphi_{i-1/2,j} = \varphi(x_{i-1/2}, y_j)$, $\psi_{i,j-1/2} = \psi(x_i, y_{j-1/2})$, and $u_{i,j} = u(x_i, y_j)$.

Assuming for simplicity that the computational grid is square, i.e. $\Delta x_i = \Delta y_j = \Delta x,\ \forall (i,j)$, $1 \le i \le N,\ 1 \le j \le N$, we apply summation by parts to the right hand side of (10) to obtain a discrete analogue of the right hand side of (8)

$$\begin{aligned} &\Delta x \sum_{i,j} u_{i,j} \left((\varphi_{i+1/2,j} - \varphi_{i-1/2,j}) + (\psi_{i,j+1/2} - \psi_{i,j-1/2}) \right) = \\ &-\Delta x \sum_{i,j} \varphi_{i+1/2,j}(u_{i+1,j} - u_{i,j}) + \psi_{i,j+1/2}(u_{i,j+1} - u_{i,j}) = -\Delta x \sum_{i,j} \langle \boldsymbol{D} u_{i,j}, \boldsymbol{\varphi}_{i,j} \rangle, \end{aligned} \tag{11}$$

where $\langle \cdot, \cdot \rangle$ denotes the Euclidean inner product of vectors in $\mathbb{R}^2$, and $\boldsymbol{\varphi}_{i,j}$ and $\boldsymbol{D} u_{i,j}$ are defined below. The vector $\boldsymbol{D} u_{i,j} = (D^1 u_{i,j}, D^2 u_{i,j})$ with the components

$$D^1 u_{i,j} = u_{i+1,j} - u_{i,j}, \quad D^2 u_{i,j} = u_{i,j+1} - u_{i,j}, \tag{12}$$

can be viewed as a forward difference approximation of the gradient of u at the centroid of $\Omega_{i,j}$, up to division by Δx. Alternatively, $D^1 u_{i+1/2,j}$ can be viewed as a centered approximation of the partial derivative of u with respect to x at $(x_{i+1/2}, y_j)$, the midpoint of the right edge of $\Omega_{i,j}$, and $D^2 u_{i,j+1/2}$ as the partial derivative with respect to y at $(x_i, y_{j+1/2})$, the upper edge's midpoint, up to division by Δx. Similarly, the values $\varphi_{i+1/2,j}$ and $\psi_{i,j+1/2}$ are combined into a vector, $\boldsymbol{\varphi}_{i,j} = (\varphi_{i+1/2,j}, \psi_{i,j+1/2})$. Note that though the values of φ and ψ are computed at edge midpoints, we associate $\boldsymbol{\varphi}_{i,j}$ with $\Omega_{i,j}$ and summation over i and j in (11).

Replacing the centroid values $u_{i,j}$ with $U_{i,j}$, the values of the discrete function U on each $\Omega_{i,j}$, we obtain a semi-discrete version of (9), known as Raviart-Thomas TV [5] or discrete dual total variation

$$TV_{RT}(U) = \max_{\boldsymbol{\varphi} \in C_c^1(\Omega)} \left\{ \Delta x \sum_{i,j} \langle \boldsymbol{D} U_{i,j}, \boldsymbol{\varphi}_{i,j} \rangle : \|\boldsymbol{\varphi}(x,y)\| \le 1,\ \forall (x,y) \in \Omega \right\}. \tag{13}$$

and the factor Δx before the sum accounts for the size of the cells. Since computation of the inner products in (13) requires the values of the continuous function $\boldsymbol{\varphi}$ at edge midpoints only, $\boldsymbol{\varphi}$ can be replaced with a discrete function $\widetilde{\boldsymbol{\varphi}}$, with $\widetilde{\boldsymbol{\varphi}}_{i,j} = (\varphi_{i+1/2,j}, \psi_{i,j+1/2})$ defined on the $(N+1)\times(N+1)$ grid of edge midpoints $(x_{i+1/2}, y_j)$, $(x_i, y_{j+1/2})$. To obtain a fully discrete expression for $TV_{RT}(U)$, the constraint $\|\boldsymbol{\varphi}(x,y)\| \le 1$ on $\boldsymbol{\varphi}$ should be replaced with an equivalent constraints on values of $\widetilde{\boldsymbol{\varphi}}$. In [4, 7, 16], this idea has been extensively studied and used to construct fully discrete dual TV definitions for TV-regularization based optimization with application to imaging problems.

There are multiple ways to impose the bound on the norm of the discrete test function $\widetilde{\boldsymbol{\varphi}}$. An obvious constraint results from the bounds on the values of $\boldsymbol{\varphi}$ at edge midpoints, i.e. $\sqrt{\varphi^2_{i+1/2,j} + \psi^2_{i+1/2,j}} \le 1$ and $\sqrt{\varphi^2_{i,j+1/2} + \psi^2_{i,j+1/2}} \le 1$. However, by the derivation above $\psi_{i+1/2,j}$ and $\varphi_{i,j+1/2}$ are not included in $\widetilde{\boldsymbol{\varphi}}$. Since these values are not available, they need to be defined outside of the definition (13). We interpolate them by averaging. For example, the value of $\psi_{i+1/2,j}$ on a uniform grid can be obtained by averaging $\psi_{i,j+1/2}, \psi_{i+1,j+1/2}, \psi_{i,j-1/2}, \psi_{i+1,j-1}$, as

$$\psi_{i+1/2,j} = \frac{\psi_{i,j+1/2} + \psi_{i,j-1/2} + \psi_{i+1,j+1/2} + \psi_{i+1,j-1/2}}{4},$$

see Figure 1 and Figure 2 (right). We can write this in operator notation by setting $(\varphi_{i+1/2,j}, \psi_{i+1/2,j}) \equiv (\boldsymbol{P}^1\widetilde{\boldsymbol{\varphi}})_{i+1/2,j}$ where

$$(\boldsymbol{P}^1\widetilde{\boldsymbol{\varphi}})_{i+1/2,j} = \left((P^1\widetilde{\boldsymbol{\varphi}})^1_{i+1/2,j}, (P^1\widetilde{\boldsymbol{\varphi}})^2_{i+1/2,j}\right) = \left(\varphi_{i+1/2,j}, \quad \frac{\psi_{i,j+1/2} + \psi_{i,j-1/2} + \psi_{i+1,j+1/2} + \psi_{i+1,j-1/2}}{4}\right). \tag{14}$$

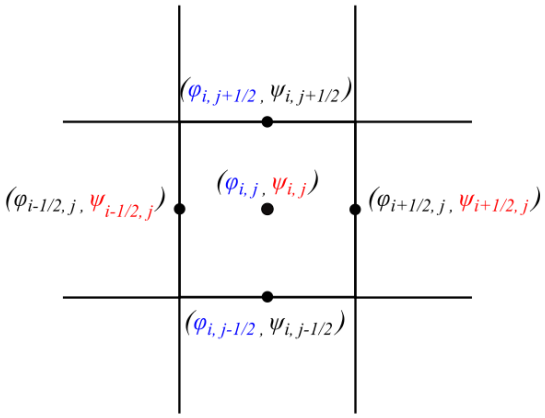

FIGURE 1. The stencil of the discrete test function in the dual definition (17) on $\Omega_{i,j} = [x_{i-1/2}, x_{i+1/2}] \times [y_{j-1/2}, y_{j+1/2}]$. Components of $\widetilde{\boldsymbol{\varphi}}$ are shown in black. Interpolated values are shown in red and blue.

In $\boldsymbol{P}^1(\widetilde{\boldsymbol{\varphi}})$, the first component is the identity operator and the second component averages the values of ψ on the four horizontal edges around the point $(x_{i+1/2}, y_j)$ and assigns this value to $\psi_{i+1/2,j}$, see Figure 2 (right). Similarly, we define $(\varphi_{i,j+1/2}, \psi_{i,j+1/2}) \equiv (\boldsymbol{P}^2\widetilde{\boldsymbol{\varphi}})_{i,j+1/2}$, where the first component is the average of the values of φ on the four vertical edges around the point $(x_i, y_{j+1/2})$ and the second component is the identity operator, see Figure 2 (left). Finally, we define the centroid value $(\varphi_{i,j}, \psi_{i,j}) \equiv (\boldsymbol{P}^3\widetilde{\boldsymbol{\varphi}})_{i,j}$, as an average of edge values in the horizontal and vertical directions, see Figure 2 (center). The operators

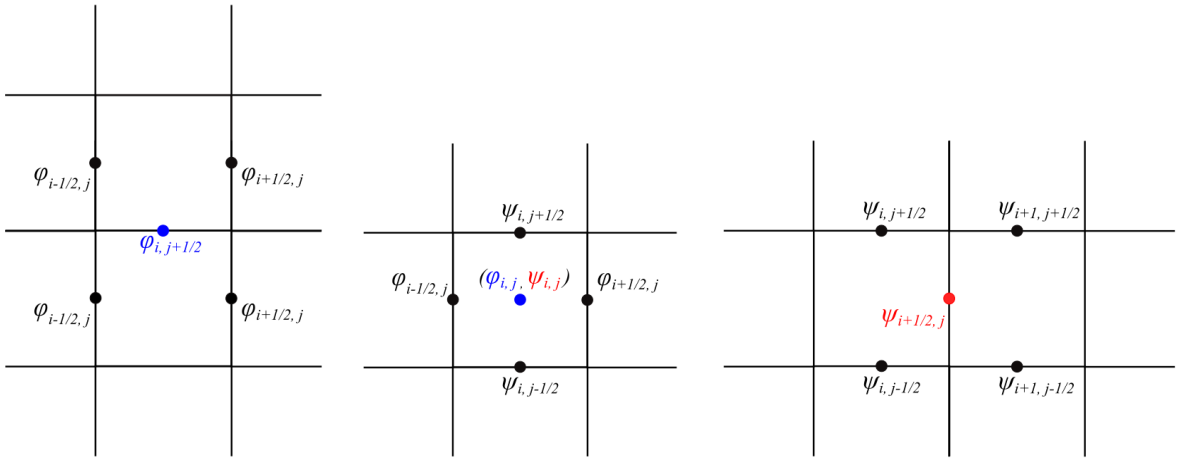

FIGURE 2. Interpolation stencils for $\varphi_{i,j+1/2}$ (left), $\varphi_{i,j}, \psi_{i,j}$ (center), $\psi_{i+1/2,j}$ (right). Components of $\widetilde{\boldsymbol{\varphi}}$ are shown in black, interpolated values are shown in red and blue.

$\boldsymbol{P}^2$ and $\boldsymbol{P}^3$ are defined as

$$(\boldsymbol{P}^2\widetilde{\boldsymbol{\varphi}})_{i,j+1/2} = \left((P^2\widetilde{\boldsymbol{\varphi}})^1_{i,j+1/2}, (P^2\widetilde{\boldsymbol{\varphi}})^2_{i,j+1/2}\right) = \left(\frac{\varphi_{i+1/2,j} + \varphi_{i+1/2,j+1} + \varphi_{i-1/2,j} + \varphi_{i-1/2,j+1}}{4}, \quad \psi_{i,j+1/2}\right), \tag{15}$$

$$(\boldsymbol{P}^3\widetilde{\boldsymbol{\varphi}})_{i,j} = \left((P^3\widetilde{\boldsymbol{\varphi}})^1_{i,j}, (P^3\widetilde{\boldsymbol{\varphi}})^2_{i,j}\right) = \left(\frac{\varphi_{i+1/2,j} + \varphi_{i-1/2,j}}{2}, \quad \frac{\psi_{i,j+1/2} + \psi_{i,j-1/2}}{2}\right). \tag{16}$$

Since $\boldsymbol{\varphi}$ was assumed to satisfy $(\boldsymbol{\varphi}\cdot\vec{\boldsymbol{n}}) = 0$ on $\partial\Omega$, we require $(\widetilde{\boldsymbol{\varphi}}\cdot\vec{\boldsymbol{n}}) = 0$, which means that the boundary values of $\widetilde{\boldsymbol{\varphi}}$ are equal zero, i.e. $\varphi_{1/2,j} = \varphi_{N+1/2,j} = \psi_{i,1/2} = \psi_{i,N+1/2} = 0$, $0 \le i \le N$, $0 \le j \le N$. With that, we define the space

$$\boldsymbol{\Pi}(\Omega) = \{\widetilde{\boldsymbol{\varphi}} \in \mathbb{R}^{2\times(N+1)\times(N+1)} : (\widetilde{\boldsymbol{\varphi}} \cdot \vec{\boldsymbol{n}}) = 0 \text{ on } \partial\Omega\}.$$

Then, using the constraints and notations developed above, we arrive at a fully discrete expression for the dual total variation [7]

$$TV_d(U) = \max_{\widetilde{\boldsymbol{\varphi}}\in\boldsymbol{\Pi}(\Omega)} \left\{ \Delta x \sum_{i,j} \langle \boldsymbol{D}U_{i,j}, \widetilde{\boldsymbol{\varphi}}_{i,j}\rangle : \sqrt{\varphi^2_{i+1/2,j} + \psi^2_{i+1/2,j}} \le 1, \ \sqrt{\varphi^2_{i,j+1/2} + \psi^2_{i,j+1/2}} \le 1, \right.$$
$$\left. \sqrt{\varphi^2_{i,j} + \psi^2_{i,j}} \le 1, \ \forall (i,j) \right\}, \tag{17}$$

where the subscript d stands for "dual". Using the operator notation (14) - (16), the above can be rewritten as

$$TV_d(U) = \max_{\widetilde{\boldsymbol{\varphi}}\in\boldsymbol{\Pi}(\Omega)} \left\{ \Delta x \sum_{i,j} \langle \boldsymbol{D}U_{i,j}, \widetilde{\boldsymbol{\varphi}}_{i,j}\rangle : \|\boldsymbol{P}^k\widetilde{\boldsymbol{\varphi}}\|_2 \le 1, \ k = 1,\dots,3, \ \forall (i,j) \right\}, \tag{18}$$

where $\|\cdot\|_2$ denotes the Euclidean norm of a vector $(\boldsymbol{P}^k\widetilde{\boldsymbol{\varphi}})_{i,j}$ in $\mathbb{R}^2$.

Computing the maximizer of the constrained optimization problem (18) is a difficult task. Therefore, an equivalent saddle-point formulation [22] is derived. For this purpose, we will state the primal-dual formulation of (18). We introduce the gradient field $\boldsymbol{v} = (\boldsymbol{v}_1, \boldsymbol{v}_2, \boldsymbol{v}_3)$, with $\boldsymbol{v}_k = (v^x_k, v^y_k) \in \mathbb{R}^2$, $k = 1, 2, 3$, approximating ∇u at $(x_{i+1/2}, y_j)$, $(x_i, y_{j+1/2})$ and (x_i, y_j), respectively. Let $\boldsymbol{v} \in \boldsymbol{V}$, where

$$\boldsymbol{V} = \{\boldsymbol{v} : \|\boldsymbol{v}\|_{1,1,2} < +\infty\}, \ \|\boldsymbol{v}\|_{1,1,2} = \sum_k \|\boldsymbol{v}_k\|_{1,2}, \ \|\boldsymbol{v}_k\|_{1,2} = \sum_{i,j} \|(\boldsymbol{v}_k)_{i,j}\|_2 = \sum_{i,j} \sqrt{(v^x_k)^2_{i,j} + (v^y_k)^2_{i,j}}.$$

We define the operator $\boldsymbol{F}: \boldsymbol{V} \to \mathbb{R}^{2\times(N+1)\times(N+1)}$: $(\boldsymbol{F}\boldsymbol{v})_{i,j} = ((F^1\boldsymbol{v})_{i+1/2,j}, (F^2\boldsymbol{v})_{i,j+1/2})$, with components

$$(F^1\boldsymbol{v})_{i+1/2,j} = \left((v_1^x)_{i+1/2,j} + \frac{(v_2^x)_{i,j+1/2} + (v_2^x)_{i,j-1/2} + (v_2^x)_{i+1,j+1/2} + (v_2^x)_{i+1,j-1/2}}{4} + \frac{(v_3^x)_{i,j} + (v_3^x)_{i+1,j}}{2}\right), \tag{19}$$

$$(F^2\boldsymbol{v})_{i,j+1/2} = \left((v_2^y)_{i+1/2,j} + \frac{(v_1^y)_{i+1/2,j} + (v_1^y)_{i+1/2,j+1} + (v_1^y)_{i-1/2,j} + (v_1^y)_{i-1/2,j+1}}{4} + \frac{(v_3^y)_{i,j} + (v_3^y)_{i,j+1}}{2}\right). \tag{20}$$

The operator $\boldsymbol{F}$ is a projection of $\boldsymbol{v}$ onto a coarser grid of edge midpoints. The value of the first component $(F^1\boldsymbol{v})_{i+1/2,j}$ is assigned to the edge midpoint $(x_{i+1/2}, y_j)$ and the value of the second component $(F^2\boldsymbol{v})_{i,j+1/2}$ to the edge midpoint $(x_i, y_{j+1/2})$. Then, the primal-dual formulation of (18) can be stated as the following saddle-point problem

$$TV_d(U) = \min_{\boldsymbol{v}\in\boldsymbol{V}} \max_{\widetilde{\boldsymbol{\varphi}}\in\boldsymbol{\Pi}(\Omega)} \left\{ \Delta x \sum_{i,j} \langle\, (\boldsymbol{F}\boldsymbol{v})_{i,j}, \widetilde{\boldsymbol{\varphi}}_{i,j}\rangle : \boldsymbol{F}\boldsymbol{v} = \boldsymbol{D}U,\ \|\boldsymbol{P}^k\widetilde{\boldsymbol{\varphi}}\|_2 \le 1,\ k=1,2,3,\ \forall(i,j) \right\}. \tag{21}$$

Using (21), we can derive a minimization problem for $\boldsymbol{v}$, an approximation of the gradient of u,

$$TV_d(U) = \min_{\boldsymbol{v}\in\boldsymbol{V}} \left\{ \Delta x \left(\sum_{i,j} \|(\boldsymbol{v}_1)_{i,j}\|_2 + \sum_{i,j} \|(\boldsymbol{v}_2)_{i,j}\|_2 + \sum_{i,j} \|(\boldsymbol{v}_3)_{i,j}\|_2 \right) : \boldsymbol{F}\boldsymbol{v} = \boldsymbol{D}U \right\}. \tag{22}$$

The above is called the primal problem, for which (18) is the corresponding dual problem.

There are generally infinitely many ways to define $\boldsymbol{P}^k$ and corresponding $\boldsymbol{F}$. A proper choice of operators $\boldsymbol{P}^k, \boldsymbol{F}$ allows one to establish the uniqueness of the maximizer $\widetilde{\boldsymbol{\varphi}}$ in (18) and consistency of the resulting discrete dual TV definition with the analytical TV (3). We now appeal to a general theorem of [4], which states

Theorem 2.1. *Assume the supports and the weights of the convolutions defining operators $\boldsymbol{F}$ on the $N \times N$ meshes are uniformly bounded. Then discrete dual TV defined by*

$$TV(U) = \min_{\boldsymbol{v}} \{\Delta x \|\boldsymbol{v}\| : \boldsymbol{F}\boldsymbol{v} = \boldsymbol{D}U\}, \tag{23}$$

where the norm is taken in an appropriate space, Γ-converges to

$$TV(U) = \begin{cases} |Du|(\Omega) & \text{if } u \in BV(\Omega), \\ +\infty & \text{otherwise .} \end{cases} \tag{24}$$

The convergence holds in both weak and strong topologies, such as $L_p(\Omega)$ for any $p < +\infty$.

The following result is the direct implication of Theorem 2.1

Corollary 2.1.1. *The discrete TV defined by* (17) *is consistent with* (3) *in the sense of* (24).

Furthermore, the compactness result for TV_d follows from Proposition 2.5 of [4]. Let $\{U^N\}_{N>0}$ be a sequence of discrete functions, defined on $N \times N$ grids. Let us further assume that

$$TV_d(U^N) < +\infty,\ \forall N > 0,$$

and that U^N remains bounded in $L_p(\Omega)$. Then there exists a subsequence $\hat{U}^N$ of U^N and a function $u \in L_1(\Omega)$, such that $\hat{U}^N$ converges to u in $L_1(\Omega)$.

By Proposition 1 of [7], a strong duality between (18) and (22) holds. Therefore, the primal and dual problems have the same optimal value. That is, if a maximizer $\widetilde{\boldsymbol{\varphi}}^\dagger$ of the primal problem and a minimizer $\boldsymbol{v}^\dagger$ of the dual problem exist, then we have

$$TV_d(U) = \Delta x \sum_{i,j} \langle\, \boldsymbol{D}U_{i,j}, \widetilde{\boldsymbol{\varphi}}^\dagger_{i,j}\rangle = \Delta x \|\boldsymbol{v}^\dagger\|_{1,1,2}.$$

We compute the minimizer $\boldsymbol{v}^\dagger$ using the alternating proximal gradient method ([7], Algorithm 2), a simplified version of the general alternating direction method of multipliers. The algorithm is given below.

Algorithm 1 To solve (18)-(22) for $\boldsymbol{v}^\dagger, \widetilde{\boldsymbol{\varphi}}^\dagger$, given U on a square mesh.

$\boldsymbol{v}^0 := ((D^1U, \mathbf{0}), (\mathbf{0}, D^2U), (\mathbf{0}, \mathbf{0})), \quad \widetilde{\boldsymbol{\varphi}}^0 := \mathbf{0}$
while $|\|\boldsymbol{v}^{n+1}\|_{1,1,2} - \|\boldsymbol{v}^n\|_{1,1,2}| > \varepsilon$ **do**
  for $k = 1 \dots 3$ **do**
    $\boldsymbol{v}_k^{n+1} = (\boldsymbol{v}_k^n + \gamma \boldsymbol{P}^k(\boldsymbol{D}U - \boldsymbol{F}\boldsymbol{v}^n + \mu\widetilde{\boldsymbol{\varphi}}^n))(1 - 1/[max(|\boldsymbol{v}_k^n|/\gamma\mu, 1)])$
    $\widetilde{\boldsymbol{\varphi}}^{n+1} = \widetilde{\boldsymbol{\varphi}}^n + (\boldsymbol{D}U - \boldsymbol{F}\boldsymbol{v}^{n+1})/\mu$
  end for
end while

In Algorithm 1, $\boldsymbol{P}^k$, $k = 1, 2, 3$, are defined by (14)-(16) and $\boldsymbol{D}U$ is given by (12). The algorithm converges when $\gamma\|\boldsymbol{F}\|^2 < 1$ and $\mu > 0$ [4], where $\|\boldsymbol{F}\|$ is the operator norm of $\boldsymbol{F}$ and $\|\boldsymbol{F}\|^2 \le 3$. Suitable values for the parameter μ are discussed in Section 3, while $\gamma = 0.33$ is used as suggested in [7].

3. Accuracy of discrete TV definitions

Before applying the three definitions of discrete TV introduced in the previous sections to numerical solutions of hyperbolic PDEs, we investigate how well discrete TVs approximate the analytical TV (3) under mesh refinement and verify convergence of the Algorithm 1.

3.1. **Asymptotic consistency.** We consider a rectangular domain $\Omega = [-1, 1] \times [-1, 1]$ and a function $u(x, y) = \exp\left(-\frac{x^2+y^2}{.15^2}\right)$. Ω is discretized into an $N \times N$ mesh of square elements $\Omega_{i,j}$. We approximate u by a grid-based function U, where $U_{i,j}$ is set equal to the cell average of u on $\Omega_{i,j}$. $TV_a(U)$ and $TV_{is}(U)$ are computed using (5) and (7), respectively. $TV_d(U)$ is computed according to Algorithm 1 with $\varepsilon = 10^{-7}$, which is a sufficient accuracy for the examples considered here and later on in Section 4. The TV values obtained using the three definitions are listed in Table 1. Next, we compare them to the analytical TV of $u(x, y)$ given by (4)

$$TV(u) = \int_\Omega \sqrt{u_x^2 + u_y^2}\, dxdy \approx 0.835249.$$

It appears that $TV_d(U)$ and $TV_{is}(U)$ converge to $TV(u)$ as N increases, while $TV_a(U)$ approaches the value of the integral in (6), i.e. $TV_a(u) \approx 1.063472$ at the limit of $\Delta x \to 0$, $\Delta y \to 0$ for this smooth u.

N	TV_a	ΔTV_a	TV_{is}	ΔTV_i	TV_d	ΔTV_d	μ
20	1.109121	0.045649	0.868625	0.033347	0.874901	0.039749	5.0e-1
40	1.088240	0.024768	0.854071	0.018782	0.855026	0.019873	3.0e-1
80	1.076348	0.012876	0.845162	0.009981	0.845381	0.010022	1.0e-1
160	1.069985	0.006513	0.840318	0.005069	0.840308	0.005059	5.0e-2

Table 1. Total variation of discrete approximations U of $u(x, y) = \exp\left(-\frac{x^2+y^2}{.15^2}\right)$ on $N = 20, 40, 80, 160$ meshes.

We report the magnitude of the difference between the analytical and discrete TVs, denoted by ΔTV, in Table 1. We observe that for this smooth function, the TV_{is} and TV_d converge linearly to $TV(u)$, and TV_a converges linearly to $TV_a(u)$.

Remark. Convergence of Algorithm 1 depends on a proper choice for the value of parameter μ [7]. In particular, we have observed in our numerical experiments that μ dependents on the size of a mesh and for a carefully tuned value of μ the convergence of ΔTV_d can be superlinear. To find a suitable value for a mesh of a particular resolution, we ran a direct search in the interval $(0, 1)$ with a step size $\Delta\mu = 5.0 \times 10^{-2}$. We choose the value of μ that provides the smallest ΔTV_d. The number of steps to convergence also depends on mesh size. For example, it took $50 - 100$ iterations to achieve the $\varepsilon = 10^{-7}$ accuracy with $N = 80$. The values of μ found for each mesh are listed in the last column of Table 1. These values were also used in the numerical tests in Section 4.

3.2. **Spatial isotropy.** Next, we investigate how discrete TV of a discontinuous shape varies when the shape is rotated. We consider a rectangular domain $\Omega = [-2, 2] \times [-2, 2]$ and a square pulse defined on Ω by

$$u(x, y) = \begin{cases} 1, & \text{if } x \in [-1/\sqrt{2}, 1/\sqrt{2}], \quad y \in [-1/\sqrt{2}, 1/\sqrt{2}], \\ 0, & \text{otherwise.} \end{cases} \tag{25}$$

Similar to the previous example, $U_{i,j}$ is set equal to the cell average of u on $\Omega_{i,j}$, an element in a uniform, $N \times N$ mesh of Ω with $\Delta x = \Delta y = 4/N$. To simplify calculations, we choose N to be a multiple of 4. The resulting discrete function with $N = 40$ is illustrated in Figure 3 (A). $U_{i,j}$ takes three distinct values: $U_{i,j} = 1$ in the interior of the square, $U_{i,j} = \{N/(4\sqrt{2})\}$ on the elements containing the edges of $u(x, y)$ and $U_{i,j} = \{N/(4\sqrt{2})\}^2$ on the elements containing the corners. Here, $\{\cdot\}$ denotes the fractional part of a real number. It follows from (5) that

$$TV_a(U) = 4(2\lfloor N/(4\sqrt{2})\rfloor + 2\{N/(4\sqrt{2})\})\Delta x,$$

where $\lfloor\cdot\rfloor$ is the floor function of a real number. Under mesh refinement, i.e. as $N \to \infty$, $TV_a(U)$ tends to $4\sqrt{2}$. Using (7), it is straightforward to show that $TV_{is}(U)$ also converges to $4\sqrt{2}$ as $N \to \infty$. Finally, we evaluate $TV_d(U)$ numerically using Algorithm 1. We tabulate the values of TV according to the three definitions in Table 2. We observe that $TV_a(U)$, $TV_{is}(U)$, and $TV_d(U)$ converge to $4\sqrt{2} \approx 5.656854$ under mesh refinement.

N	$TV_a(U)$	$TV_{is}(U)$	$TV_d(U)$	$TV_a(V)$	$TV_{is}(V)$	$TV_d(V)$	δTV_d
20	5.112478	5.027950	5.075765	7.200000	6.099066	5.856872	0.781107
40	5.391645	5.340205	5.362765	7.600000	6.172694	5.754304	0.391539
80	5.525928	5.491928	5.501844	7.800000	6.208110	5.704962	0.203118
160	5.591803	5.570904	5.576312	7.900000	6.225484	5.680757	0.104445

TABLE 2. TV values for the square pulse U and the rotated square pulse V, $\delta TV_d = |TV_d(U) - TV_d(V)|$.

Next, we consider the function $v(x, y) = u(x\cos\theta + y\sin\theta, -x\sin\theta + y\cos\theta)$, which corresponds to counterclockwise rotation of u by the angle θ. Since rotation does not change analytical TV of u according to (3), we have $TV(v) = TV(u)$. Choosing $\theta = \pi/4$, we obtain a square shape whose diagonals are aligned with the coordinate axes. Using the same meshes as above, we construct discrete functions V from v (Figure 3 (B)). $V_{i,j}$ takes three values: 0 in the exterior of the square, 1 in the interior, and 0.5 on the elements containing edges of v. The explicitly calculated value of the TV_a is

$$TV_a(V) = (2N - 4)\Delta x = 8 - 16/N,$$

which tends to 8 as $N \to \infty$. Then, $TV_a(V)$ is greater than $TV_a(U) = 4\sqrt{2}$ by a factor of $\sqrt{2}$. The value for the $TV_{is}(V)$

$$TV_{is}(V) = ((3\sqrt{2} + 2)N/4 - 5\sqrt{2}/2 + 2)\Delta x,$$

converges to $3\sqrt{2} + 2 \approx 6.24$, as $N \to \infty$, which is greater than the $TV_{is}(U) = 4\sqrt{2}$ by a factor of $(3 + \sqrt{2})/4 \approx 1.1$.

We observe that $TV_a(U) \neq TV_a(V)$, $TV_{is}(U) \neq TV_{is}(V)$, $TV_d(U) \neq TV_d(V)$ on the same mesh. This is expected because U and V are different projections of u on a finite mesh. However, we would like to see convergence between these values under mesh refinement. TV values according to the three definitions are listed in Table 2. We notice that $TV_d(V)$ is the only one such that $\delta TV = |TV_d(U) - TV_d(V)|$, i.e. the difference in TV values between the original and rotated functions, diminishes as N increases.

We conclude that both TV_a and TV_{is} values change when the shape is rotated, while TV_d does not. Thus, neither TV_a, nor TV_{is} are isotropic.

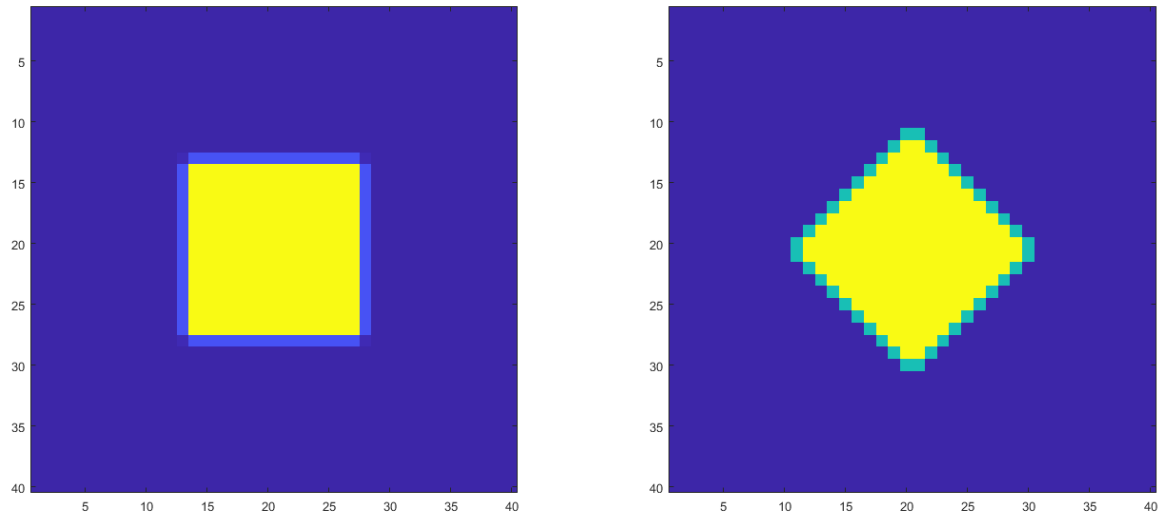

(A) Function U, square pulse

(B) Function V, rotated square pulse

FIGURE 3. Projection of the square pulse onto 40-by-40 mesh.

4. Numerical Examples

In this section, we present a number of numerical examples, whose aim is to demonstrate that the second order DG method is TVD in the TV_d sense and is not TVD in the TV_a and TV_i sense. In discretizing the spatial variable, we used the tensor-product, orthogonal basis functions of degree one. The system of ODEs resulted from the DG spatial discretization was solved with the Heun's time integrator. We employed the moment limiter, introduced in [17]. All problems were solved on a square domain $\Omega = [-1, 1] \times [-1, 1]$ discretized into square cell, $N \times N$ meshes.

We computed the total variation of the obtained solutions using the conventional TV_a, TV_{is} and dual (17) definitions, where $U_{i,j}$ is the solution average on $\Omega_{i,j}$. TV_d was calculated with Algorithm 1 and $\varepsilon = 10^{-7}$. The value of parameter τ is given in Table 1.

4.1. **Rotation of a hill.** We begin by studying rotation of a cosine hill around the origin described by

$$u_t + 2\pi x u_x - 2\pi y u_y = 0, \tag{26}$$

with the initial condition

$$u_0(x, y) = \begin{cases} \cos 2\pi r^2, & \text{for } r = \sqrt{(x - 0.25)^2 + (y - 0.25)^2} \le 0.25, \\ 0, & \text{otherwise}, \end{cases} \tag{27}$$

and suitable boundary conditions. We solve the problem with and without the limiter until the final time $t = 0.125$, which corresponds to the counter-clockwise rotation of the hill by $\pi/4$. The initial condition and solution at $t = 0.125$ on the $N = 80$ mesh are shown in Figure 4.

We compute the L_1 errors and convergence rates at $t = 0.125$ and list them in Table 3. We observe that both limited and unlimited solutions exhibit the second rate of convergence.

N	L_1 error, unlimited	L_1 error, limited	r, unlimited	r, limited
40	7.4849e-03	1.2214e-02	1.1752	0.5177
80	2.6270e-03	6.3523e-03	1.5106	0.9432
160	0.4927e-03	1.8892e-03	2.4146	1.7494
320	0.0959e-03	0.4489e-03	2.3605	2.0733

TABLE 3. Convergence history of L_1 error of the limited and unlimited solutions of Example 4.1 at $t = 0.125$.

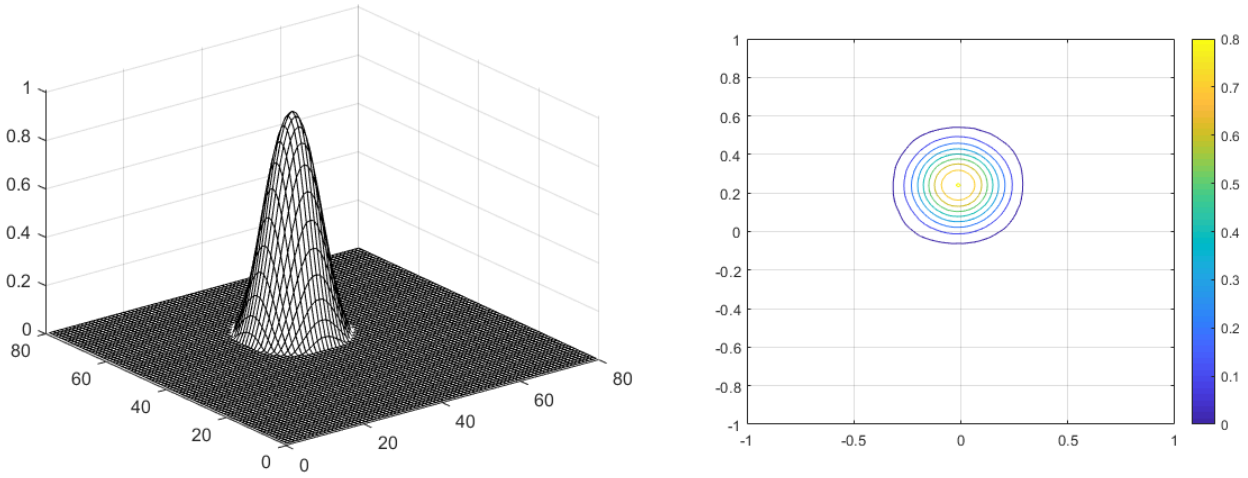

FIGURE 4. Limited solution for (26) with initial condition (27) at t = 0.125 (left) and its contour plot (right).

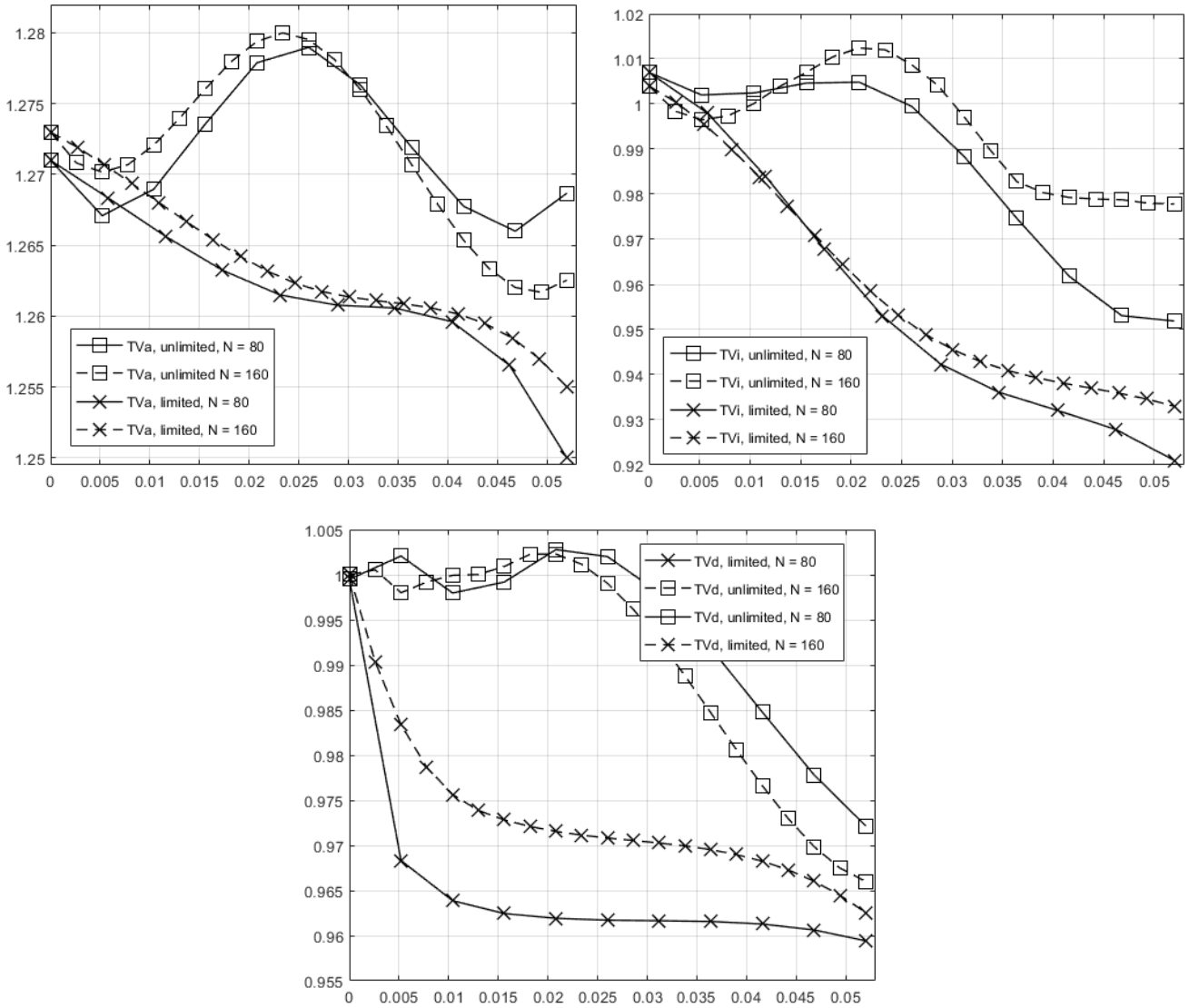

FIGURE 5. TV for solutions of (26) with the initial condition (27) for the first 10 ($N = 80$) and 20 ($N = 160$) time steps, as a function of time t.

We compute the total variation of the solutions and report the results in Table 4 and Figure 5. In Figure 5, we plot TV values of solutions computed with and without the limiter for the first 10 and 20 time steps on $N = 80$ and $N = 160$ meshes, respectively. We observe that the total variation of the limited solutions monotonically decreases with each time step for all definitions of TV. The solution on

	$N = 40$			$N = 80$			$N = 160$		
t	TV_a	TV_{is}	TV_d	TV_a	TV_{is}	TV_d	TV_a	TV_{is}	TV_d
0	1.263	1.011	1.020	1.271	1.007	0.999	1.273	1.004	1.000
0.0078	1.262	1.007	1.001	1.270	1.003	1.000	1.273	1.002	0.992
0.0156	1.271	1.007	1.000	1.279	1.003	0.999	1.280	1.013	1.001
0.0313	1.265	0.982	0.999	1.273	0.978	0.998	1.272	0.986	0.993
0.0469	1.258	0.957	0.979	1.266	0.953	0.978	1.262	0.979	0.970
0.0625	1.239	0.940	0.951	1.248	0.936	0.950	1.258	0.971	0.956
0.0781	1.221	0.928	0.931	1.229	0.924	0.930	1.239	0.956	0.942
0.0938	1.197	0.922	0.924	1.205	0.918	0.921	1.221	0.945	0.936
0.1094	1.177	0.920	0.919	1.185	0.916	0.918	1.205	0.936	0.932
0.1250	1.156	0.918	0.915	1.163	0.914	0.914	1.184	0.932	0.929

TABLE 4. Total variation values for the unlimited solutions for Example 4.1 on $N = 40, 80, 160$ meshes.

the coarser mesh is more diffusive and is more affected by the limiter. Consequently, its TV decreases faster.

The TV of the unlimited solutions behaves differently for TV_a, TV_{is} and TV_d. TV_d initially oscillates about the exact value of one and then decays. This is expected of unlimited high-order methods, with TV changes on the order of discretization error from one time step to another. Moreover, a similar behavior was reported for one-dimensional problems in [17]. The TV_a and TV_{is} initially increase and then decay, but the initial increase is a magnitude larger that in TV_d.

We further report TV for the unlimited solutions at ten time instances between $t = 0$ and $t = 0.125$ in Table 4. For this problem with a radial symmetry of the initial profile, we observe that all three TV share similar long-term behaviour. We also notice that TV_a is not a good approximation of $TV(u)$ value, as was discussed in Section 3.

Next, we solve (26) with the initial condition

$$u_0(x, y) = \begin{cases} \cos 2\pi(0.5x^2 + 1.5y^2), & \text{for } 0.5x^2 + 1.5y^2 \leq 0.25, \\ 0, & \text{otherwise,} \end{cases} \tag{28}$$

that models a hill whose level curves are ellipses. In Figure 6, we plot TV values for the limited solutions for the first 10 and 20 time steps on $N = 80$ and $N = 160$ meshes, respectively. We observe that for this asymmetric shape, the limited solutions lose the TVD property in the TV_a sense, while their TV_{is} and TV_d monotonically diminish with time.

To conclude, this example presents a formally second-order method where TV_{is} and TV_d monotonically decrease after a limiter is applied. While we further show that the TV_{is} definition is not a suitable measure of discrete TV in the context of numerical PDEs, it works here. We attribute this to the fact that TV_{is} is a good approximation of TV of smooth functions (see Section 3).

To further establish that it is the limiter that enforces the TVD property and to further test the TV_{is} definition, we consider additional numerical examples below.

4.2. **Rotation of a square pulse.** We solve the rotation problem (26) with a square pulse as the initial condition

$$u_0(x, y) = \begin{cases} 1, & \text{if } x \in [-0.25, 0.25], \quad y \in [-0.25, 0.25], \\ 0, & \text{otherwise.} \end{cases} \tag{29}$$

We solve the problem with the moment limiter on the meshes with $N = 40, 80, 160$. The solution on the $N = 80$ mesh at $t = 0.125$ is shown in Figure 7. Because the DG scheme without a limiter will produce spurious oscillations near solution discontinuities, which in turn will lead to large increases in the values of TV according to all three definitions, we omit the use of the unlimited DG here.

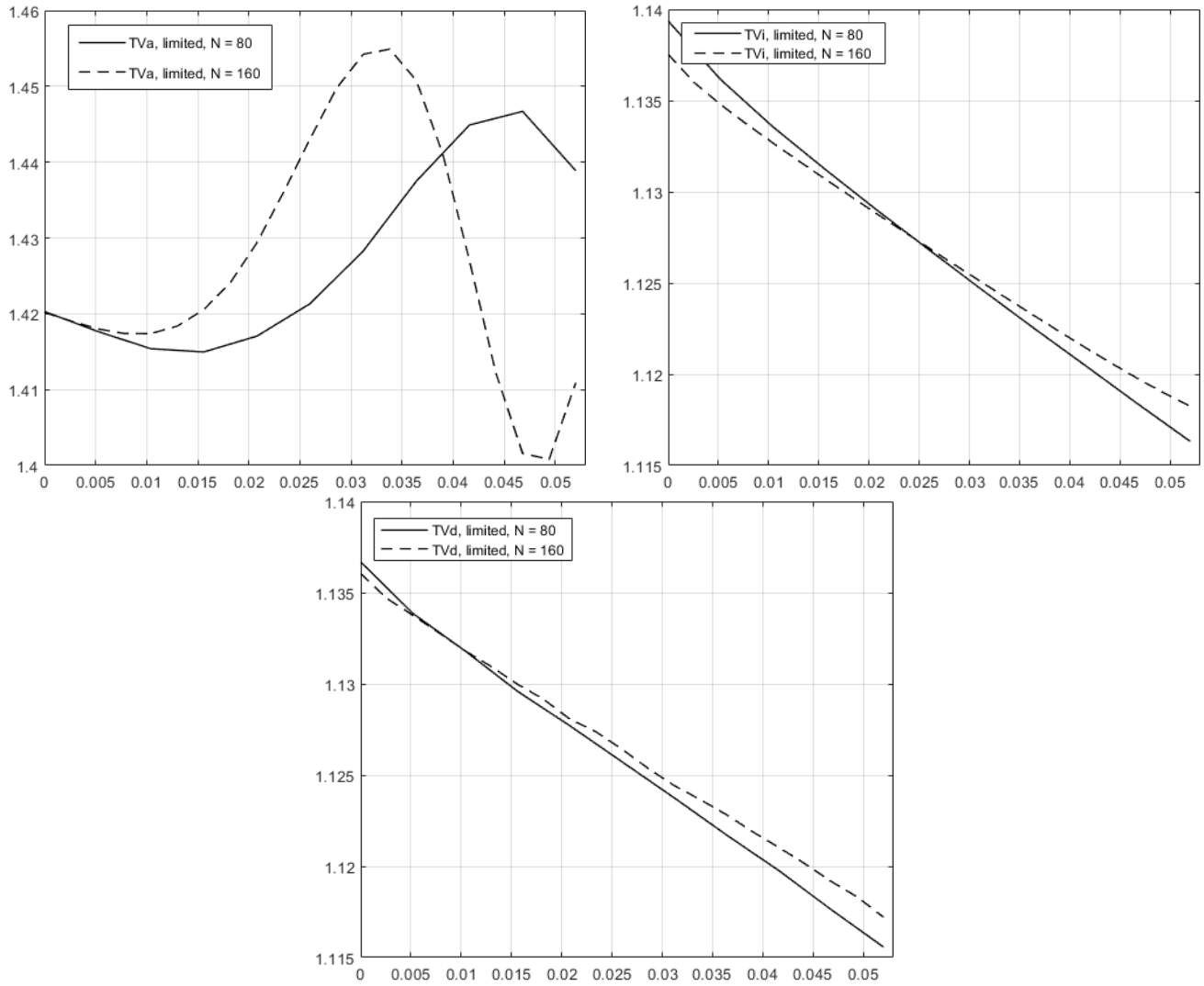

FIGURE 6. TV for the limited solutions of (26) with the initial condition (28) for the first 10 ($N = 80$) and 20 ($N = 160$) time steps, as a function of time t.

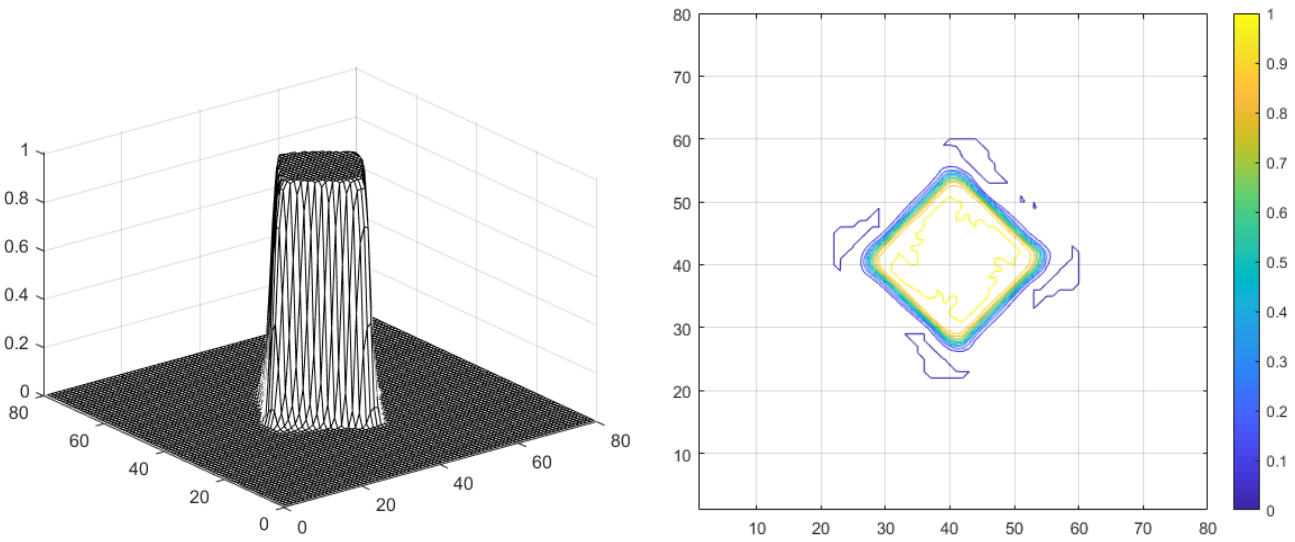

FIGURE 7. Solution for Example 4.2 with a limited DG at $t = 0.125$ (left) and its contour plot (right).

We plot the values of the discrete TV for the first 10 ($N = 80$) and 20 ($N = 160$) time steps in Figure 8 (right). The TV on the interval $t \in [0, 1]$ is shown in Figure 8 (left). We observe that the TV_a values do not decrease with time. In fact, there are intervals with marked increases in TV. The plot has a scallop-like shape with the peaks corresponding to rotation by $\pi/4$, $3\pi/4$, etc. and troughs

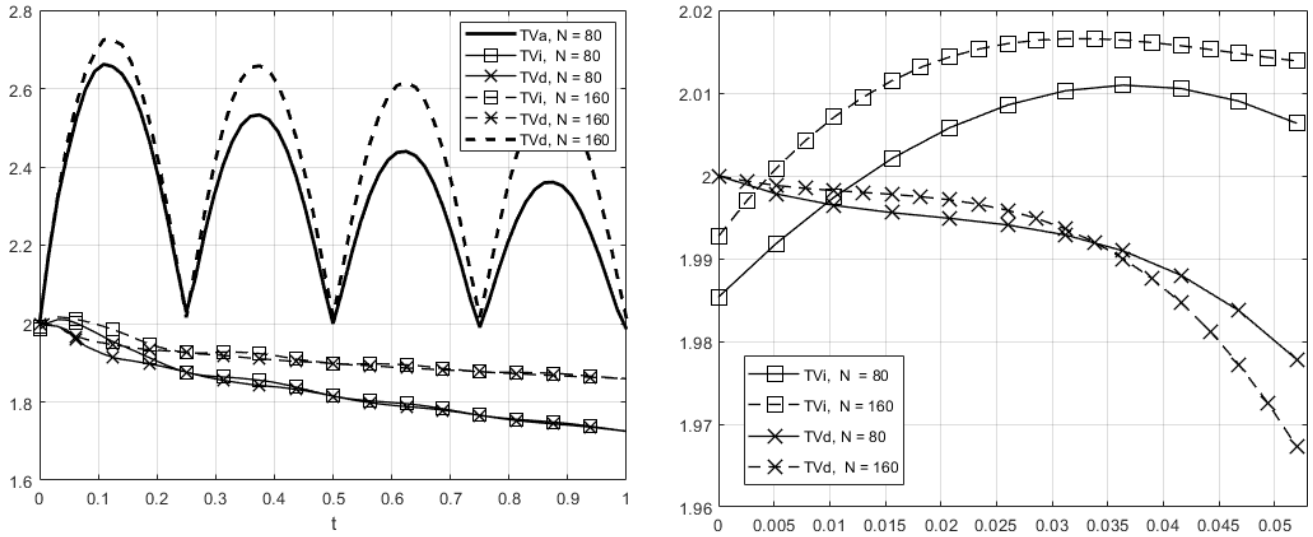

FIGURE 8. Left: TV for solution of Example 4.2 for one full rotation, which corresponds to $t \in [0, 1]$. Right: zoom for TV_{is}, TV_d of the first 10 ($N = 80$) and 20 ($N = 160$) time steps. The horizontal axis depicts time t.

corresponding to rotation by $\pi/2$, π, etc. This demonstrates the behaviour of the TV_a discussed in Section 3. That is, the computed TV_a value at the first peak is greater than that at the initial moment by a factor approaching $\sqrt{2}$, as we observe an increase of the peak values with mesh refinement. The decrease of the peak values with time can be attributed to numerical diffusion and spreading of the solution.

The plot of the TV_{is} shows a similar behaviour. The value of TV_{is} grows in time intervals $[0, 0.03125]$, $[0.25, 0.3125]$, and then again in $[0.5313, 0.5718]$. Thus, the scheme is not TVD in the TV_a and TV_{is} sense, even when a limiter is employed.

Finally, the values of the dual TV form a monotonically decreasing sequence (Table 5 and Figure 8). The limited solution is oscillation-free (Figure 7) and is TVD in means in the TV_d sense.

	$N = 40$			$N = 80$			$N = 160$		
t	TV_a	TV_{is}	TV_d	TV_a	TV_{is}	TV_d	TV_a	TV_{is}	TV_d
0	2.000	1.971	2.000	2.000	1.985	2.000	2.000	1.993	2.000
0.0156	2.148	1.944	1.954	2.177	2.002	1.996	2.180	2.012	1.998
0.0313	2.245	1.930	1.916	2.322	2.010	1.993	2.327	2.017	1.994
0.0469	2.336	1.917	1.891	2.429	2.009	1.984	2.459	2.015	1.977
0.0625	2.389	1.904	1.866	2.523	2.001	1.959	2.560	2.011	1.967
0.0781	2.435	1.886	1.848	2.597	1.990	1.943	2.641	2.005	1.960
0.0938	2.440	1.865	1.827	2.644	1.978	1.932	2.689	1.999	1.954
0.1094	2.452	1.844	1.813	2.662	1.966	1.922	2.725	1.993	1.950
0.1250	2.429	1.823	1.804	2.656	1.954	1.916	2.723	1.985	1.945

TABLE 5. Total variation values for the limited solutions for Example 4.2 on $N = 40, 80, 160$ meshes.

4.3. **Burgers' equation.** Finally, we consider the inviscid Burgers' equation

$$u_t + uu_x + uu_y = 0, \tag{30}$$

with the initial condition

$$u_0(x,y) = \begin{cases} \cos 2\pi r^2, & \text{for } r = \sqrt{(x+0.5)^2 + (y+0.5)^2} \le 0.25, \\ 0, & \text{otherwise.} \end{cases} \tag{31}$$

We solve the problem with the moment limiter for $t \in [0, 0.5]$. The solutions at $t = 0.10$, before the shock is formed at $t_S \approx 1/(2\pi)$, and $t = 0.5$ (after the shock is formed) are shown in Figure 9. Total variation values according to the three definition are shown at selected times in Table 6.

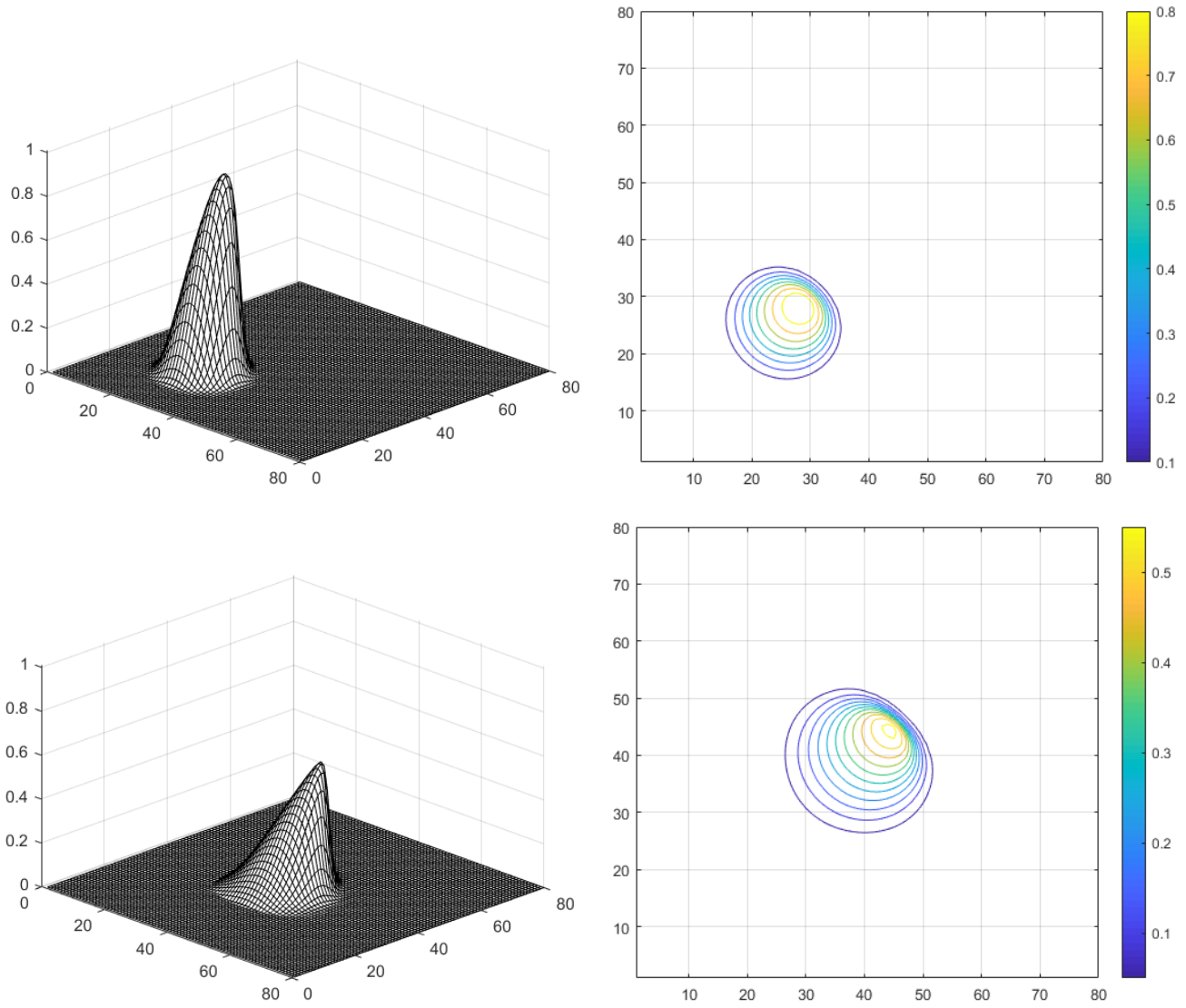

FIGURE 9. Top row: Solution for Example 4.3 with a limited DG at $t = 0.1$ (left) and its contour plot (right). Bottom row: Solution at $t = 0.5$ (left) and its contour plot (right).

Similarly to Example 4.1, we observe that TV_{is} and TV_d values monotonically decrease with time while TV_a values do not. In contrast to the previous examples, the true total variation of this problem decreases after the shock is formed due to shock/rarefaction interaction.

We notice that initially TV_a values grow due to the shape spreading of the initial profile. Then, in later times, numerical diffusion prevails and the values of TV_a dip below the initial value and continue steadily decreasing as the simulations progress. Notice that unlike in Example 4.2, the TV_{is} values do not grow with time. This is because the initial profile is translated along the main diagonal of the domain with no rotation.

5. Discussion and conclusions

We have demonstrated numerically that solutions of the second order discontinuous Galerkin method equipped with the moment limiter have the TVD property in means. The total variation of unlimited solutions might oscillate on the order of the discretization error, as expected, but also decreases with time. This holds when the total variation is measured using the fully discrete dual TV definition

	$N = 40$			$N = 80$			$N = 160$		
t	TV_a	TV_{is}	TV_d	TV_a	TV_{is}	TV_d	TV_a	TV_{is}	TV_d
0	1.271	1.007	1.003	1.273	1.004	1.001	1.273	1.002	1.000
0.0500	1.254	0.993	0.990	1.298	1.003	1.000	1.314	1.003	1.000
0.1000	1.159	0.914	0.917	1.241	0.974	0.976	1.282	1.006	0.997
0.1500	1.061	0.829	0.836	1.183	0.924	0.928	1.250	0.978	0.981
0.1592	0.971	0.758	0.763	1.124	0.875	0.880	1.214	0.947	0.951
0.1700	0.948	0.741	0.747	1.107	0.862	0.868	1.206	0.941	0.945
0.2000	0.891	0.696	0.700	1.061	0.825	0.831	1.168	0.910	0.915
0.2500	0.822	0.644	0.646	0.999	0.777	0.783	1.114	0.868	0.872
0.5000	0.678	0.531	0.529	0.780	0.609	0.609	0.895	0.699	0.702

TABLE 6. Total variation values for the limited solutions of the Burgers' equation on $N = 40, 80, 160$ meshes.

(17). Therefore, we have given an example of a scheme that is TVD, in the sense of dual discrete TV definition, and second-order accurate. This is in contrast with the long-standing result of [14], which states that any TVD scheme in two-dimensions is at most first order accurate.

We have also shown that the TV_a and TV_{is} are not suitable discrete definitions in the context of numerical methods for solution of hyperbolic PDEs. We first considered stationary examples, i.e. computing TV of the first-order L_2 projection of a function onto a square mesh. We showed that the discrete TVs converge to the analytical TVs under mesh refinement. Then we showed that TV_a and TV_{is} are not isotropic for shapes without rotational symmetry. As a result, the TV of a shape might increase or decrease under rotation. This makes these definitions not suitable for measuring TV of numerical solutions as TV increases or decreases are not fully attributed to the numerical scheme. Then we studied time-dependant DG solutions, for which we observed the increase in TV_a and TV_{is} at the beginning of computation due to the spreading of the initial shape profile. Additionally, the discrete total variation increases when an object without radial symmetry is rotated. The reason for that is the anisotropy of TV_a and TV_{is} definitions.

The next step would be to find a rigorous proof that establishes that the DGM is TVD in means in the discrete dual sense. More generally, this would entail deriving sufficient conditions on scheme coefficients (for finite-difference methods) or a limiter (for finite volumes or DGM), for the solution to satisfy the dual TVD restriction. Finally, developing a fully discrete dual TV definition for other mesh types and three-dimensional problems would be of interest.

6. ACKNOWLEDGEMENT

This work was supported in part by the Natural Sciences and Engineering Research Council of Canada grant 341373-07.

REFERENCES

[1] Feriel Abboud, Emilie Chouzenoux, Jean-Christophe Pesquet, Jean-Hugues Chenot, and Louis Laborelli. An alternating proximal approach for blind video deconvolution. *Signal Processing: Image Communication*, 70:21–36, 2019.

[2] Corentin Caillaud and Antonin Chambolle. Error estimates for finite differences approximations of the total variation. working paper or preprint, April 2020.

[3] Antonin Chambolle and Thomas Pock. Crouzeix–raviart approximation of the total variation on simplicial meshes. *Journal of Mathematical Imaging and Vision*, 62(6):872–899, 2020.

[4] Antonin Chambolle and Thomas Pock. Learning Consistent Discretizations of the Total Variation. working paper or preprint, October 2020.

[5] Antonin Chambolle and Thomas Pock. Chapter 6 - approximating the total variation with finite differences or finite elements. In Andrea Bonito and Ricardo H. Nochetto, editors, *Geometric Partial Differential Equations - Part II*, volume 22 of *Handbook of Numerical Analysis*, pages 383–417. Elsevier, 2021.

[6] Bernardo Cockburn and Chi-Wang Shu. Tvb runge-kutta local projection discontinuous galerkin finite element method for conservation laws. ii. general framework. *Mathematics of computation*, 52(186):411–435, 1989.
[7] Laurent Condat. Discrete total variation: New definition and minimization. *SIAM Journal on Imaging Sciences*, 10(3):1258–1290, 2017.
[8] Lawrence C Evans and Ronald F Gariepy. *Measure theory and fine properties of functions*, volume 5. CRC press Boca Raton, 1992.
[9] Gerald B Folland. *Real analysis: modern techniques and their applications*, volume 40. John Wiley & Sons, 1999.
[10] Andrew Giuliani and Lilia Krivodonova. Analysis of slope limiters on unstructured triangular meshes. *Journal of Computational Physics*, 374:1–26, 2018.
[11] Andrew Giuliani and Lilia Krivodonova. A moment limiter for the discontinuous galerkin method on unstructured triangular meshes. *SIAM Journal on Scientific Computing*, 41(1):A508–A537, 2019.
[12] Andrew Giuliani and Lilia Krivodonova. A moment limiter for the discontinuous Galerkin method on unstructured meshes of tetrahedra. *Journal of Computational Physics*, 404:109106, 2020.
[13] Andrew Giuliani and Lilia Krivodonova. A moment limiter for the discontinuous galerkin method on unstructured tetrahedral meshes. *Journal of Computational Physics*, 404:109106, 2020.
[14] Jonathan B Goodman and Randall J LeVeque. On the accuracy of stable schemes for 2d scalar conservation laws. *Mathematics of computation*, pages 15–21, 1985.
[15] Ami Harten. High resolution schemes for hyperbolic conservation laws. *Journal of computational physics*, 135(2):260–278, 1997.
[16] Michael Hintermüller, Carlos N Rautenberg, and Jooyoung Hahn. Functional-analytic and numerical issues in splitting methods for total variation-based image reconstruction. *Inverse Problems*, 30(5):055014, 2014.
[17] Lilia Krivodonova. Limiters for high-order discontinuous Galerkin methods. *Journal of Computational Physics*, 226(1):879–896, 2007.
[18] Dmitri Kuzmin. A new perspective on flux and slope limiting in discontinuous galerkin methods for hyperbolic conservation laws. *Computer Methods in Applied Mechanics and Engineering*, 373:113569, 2021.
[19] Randall J LeVeque. *Numerical methods for conservation laws*, volume 132. Springer, 1992.
[20] Mirko Myllykoski, Roland Glowinski, T Karkkainen, and Tuomo Rossi. A new augmented lagrangian approach for L^1-mean curvature image denoising. *SIAM Journal on Imaging Sciences*, 8(1):95–125, 2015.
[21] Kévin Polisano, Laurent Condat, Marianne Clausel, and Valérie Perrier. A convex approach to superresolution and regularization of lines in images. *SIAM Journal on Imaging Sciences*, 12(1):211–258, 2019.
[22] Ralph Tyrell Rockafellar. *Convex analysis*. Princeton university press, 2015.
[23] Leonid I Rudin, Stanley Osher, and Emad Fatemi. Nonlinear total variation based noise removal algorithms. *Physica D: nonlinear phenomena*, 60(1-4):259–268, 1992.
[24] Peter K Sweby. High resolution schemes using flux limiters for hyperbolic conservation laws. *SIAM journal on numerical analysis*, 21(5):995–1011, 1984.

Department of Applied Mathematics University of Waterloo Waterloo, Ontario Canada N2L 3G1
Email address: lgk@uwaterloo.ca

Department of Applied Mathematics University of Waterloo Waterloo, Ontario Canada N2L 3G1
Email address: a2smirno@uwaterloo.ca